Kwak et al. Chin. J. Mech. Eng. (2019) 32:83
https://doi.org/10.1186/s10033-019-0396-9

Chinese Journal of Mechanical Engineering

ORIGINAL ARTICLE

Open Access

Integrated Design of D.D.I., Filament Winding and Curing Processes for Manufacturing the High Pressure Vessel (Type II)

Hyoseo Kwak[1], Gunyoung Park[2], Hansaem Seong[2] and Chul Kim[3*]

Abstract

As energy crisis and environment pollution all around the world threaten the widespread use of fossil fuels, compressed natural gas (CNG) vehicles are explored as an alternative to the conventional gasoline powered vehicles. Because of the limited space available for the car, the composite pressure vessel (Type II) has been applied to the CNG vehicles to reach large capacity and weight lightening vehicles. High pressure vessel (Type II) is composed of a composite layer and a metal liner. The metal liner is formed by the deep drawing and ironing (D.D.I.) process, which is a complex process of deep drawing and ironing. The cylinder part is reinforced by composite layer wrapped through the filament winding process and is bonded to the liner by the curing process. In this study, an integrated design method was presented by establishing the techniques for FE analysis of entire processes (D.D.I., filament winding and curing processes) to manufacture the CNG composite pressure vessel (Type II). Dimensions of the dies and the punches of the 1st (cup drawing), 2nd (redrawing-ironing 1-ironing 2) and 3rd (redrawing-ironing) stages were calculated theoretically, and shape of tractrix die to be satisfied with the minimum forming load was suggested for life improvement and manufacturing costs in the D.D.I. process. Thickness of the composite material was determined in the filament winding process, finally, conditions of the curing process (number of heating stage, curing temperature, heating rate and time) were proposed to reinforce adhesive strength between the composite layers.

Keywords: Pressure vessel (Type II), D.D.I., Filament winding, Curing process, FEM

1 Introduction

Composite high pressure vessels are more and more frequently used in automotive industry, aviation, emergency services and power industry due to strength/stiffness-to-weight ratio [1, 2]. Because of the limited space available for the car, the composite pressure vessel (Type II) has been applied to the CNG vehicles to reach large capacity and weight lightening. There are previous studies to manufacture the vessel (D.D.I., filament winding and curing processes). They had been limited to only individual processes, but a study with respect to an integrated system dealt with entire manufacturing processes hasn't been performed yet. Karen described how to use intelligent die design based on topology optimization using a new improved differential evolution [2]. Narayanasamya dealt with the wrinkling limit diagrams of annealed three different pure sheets, using conical and tractrix dies [3]. But, it is deficient in design of the tractrix curve, which has been used in the 1st cup drawing die of the D.D.I. process, to improve die life and to reduce manufacturing costs. Geng et al. [4] derived stresses of a thick cylinder with multi-angle winding filament and proposed an optimization model of FW vessel to maximize the lowest strength ratio. Zu et al. [5] proposed a design approach for determining the optimal winding parameters of composite vessels based on non-geodesic trajectories. But they has considered only composite material, not including thickness and material properties of liner. This results in a waste of composite material due to an excessive thickness of the composite layer, and an analysis method using a coupled model with liner and composite layer

*Correspondence: chulki@pusan.ac.kr
[3] School of Mechanical Engineering, Pusan National University, Pusan 609-735, Korea
Full list of author information is available at the end of the article

© The Author(s) 2019. This article is distributed under the terms of the Creative Commons Attribution 4.0 International License (http://creativecommons.org/licenses/by/4.0/), which permits unrestricted use, distribution, and reproduction in any medium, provided you give appropriate credit to the original author(s) and the source, provide a link to the Creative Commons license, and indicate if changes were made.

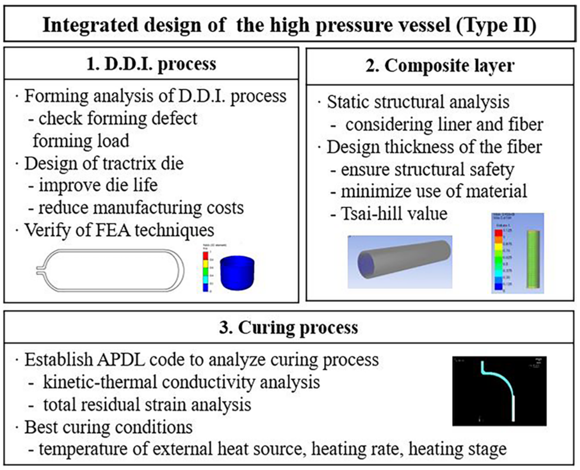

Figure 1 Configuration of the integrated design of CNG composite pressure vessel (Type II)

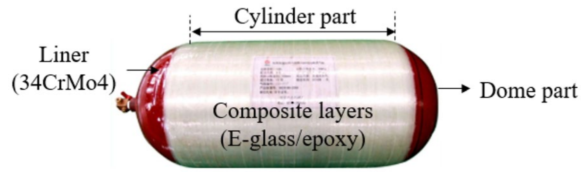

Figure 2 CNG pressure vessel (Type II)

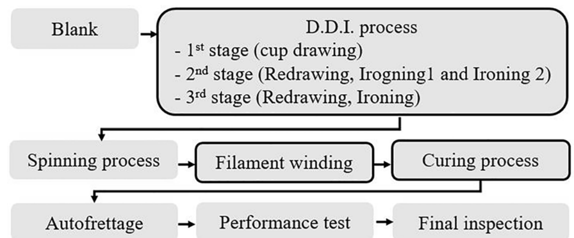

Figure 3 Manufacturing process of CNG pressure vessel (Type II)

is necessary. Minakuchi et al. [6] proposes an approach to determine material parameters for stress calculation of curing composite laminates and validate the simulation using fiber Bragg grating (FBG) strain sensors, and Li et al. [7] proposed a new cyclic heating and cooling methodology for microwave curing control of composite by analyzing mechanisms of heat conduction, stress generation and curing kinetics. But design of the curing process applying to the CNG pressure vessel (Type II) hasn't been conducted yet.

In this study, an integrated design method was presented by establishing FEA techniques of D.D.I., filament winding and curing processes to manufacture the CNG composite pressure vessel (Type II). Especially, deep drawing analysis was performed according to the heights of the tractrix die, and its shape with the minimum forming load was suggested for life improvement and reduction of manufacturing costs. Minimum thickness of the composite material to ensure a structural safety was determined considering the liner and the composite layer. Also by observation of curing degree and residual strain, conditions of the curing process were proposed to reinforce adhesive strength between the composite layers [1–3]. Configuration of the integrated design method is illustrated in Figure 1.

2 Theory of Manufacturing Process for the CNG Composite Pressure Vessel -Type II

The CNG pressure vessel (Type II), composed of a metal liner (34CrMo4) and E-glass fiber/epoxy composite wound layers as shown in Figure 2, requires different manufacturing processes to form each part: a deep drawing and ironing (D.D.I.) process for cylinder part of liner, a hot spinning process for dome part, a filament winding process to laminate the composite layers on cylinder part to endure the inner pressure, and a curing process to reinforce adhesive strength between composite layers [8].

2.1 D.D.I. Process

The D.D.I. process to form the cylinder part of liner includes a drawing process to reduce diameter of the billet and an ironing process to reduce thickness of the billet. In the 1st stage, an initial blank is fabricated into cup shape using the tractrix die to prevent a wrinkling without the blank holder. Redrawing and two ironing processes (D.I.I.) are continuously performed using the horizontal press in the 2nd stage, and finally redrawing and ironing processes (D.I.) are operated to obtain the final thickness and diameter of the liner in the 3rd stage as shown in Figure 3 [9, 10].

Theoretical design rules of the D.D.I. process are shown in Eqs. (1)–(11) [4]. The limit drawing ratios ($b_1 = 2.1$ and $b_2 = 1.35$) and tip clearance between the drawing die and the workpiece ($C_1 = 5\%$, $C_2 = 0$ and $C_3 = -5\%$) are suggested from the actual field [11]. When the dimensions of the initial blank and the final liner are given in Table 1 and Figure 4, the calculation results obtained from the above procedures are shown in Table 2 and Figure 5. Where dp_i, dd_{ij} and di_{ij} are diameters of punch, drawing die and ironing dies at ith stage and jth process. b_i, t_{ij} and A_{ij} are draw ratio, thickness of material and cross sectional area, respectively.

$$dp_1 = dm_1 - (1 + C_1) \times t_0, \tag{1}$$

$$dd_1 = dm_1 + (1 + C_1) \times t_0, \tag{2}$$

Table 1 Dimension of the initial blank and the liner

Parameter	Value
Thickness of initial blank t_0 (mm)	12.5
Diameter of initial blank D_0 (mm)	1100
Thickness of liner $t_f = t_{32}$ (mm)	4
Inner diameter of liner $D_{in} = dp_3$ (mm)	306
Outer diameter of liner D_{out} (mm)	314
Length of liner L (mm)	1830

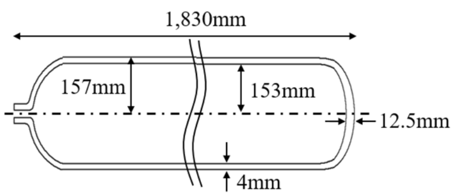

Figure 4 Dimension of the liner

Table 2 Calculation result of D.D.I. process design

1st stage (Cup drawing)					
dp_1 (mm)	510.69		b_1	2.10	
dd_1 (mm)	536.94		A_1 (mm^2)	20569.95	
2nd stage (D.I.I.)					
dp_2 (mm)	380.25		b_2	1.33	
dd_{21} (mm)	405.25	t_{21} (mm)	12.50	A_{21} (mm^2)	15423.20
di_{22} (mm)	401.19	t_{22} (mm)	10.47	A_{22} (mm^2)	12584.09
di_{23} (mm)	397.10	t_{23} (mm)	8.42	A_{23} (mm^2)	10287.97
3rd stage (D.I.)					
dp_3 (mm)	306.00		b_3	1.23	
dd_{31} (mm)	322.00	t_{31} (mm)	8.00	A_{31} (mm^2)	7893.78
di_{32} (mm)	314.00	t_{32} (mm)	4.00	A_{32} (mm^2)	3895.57

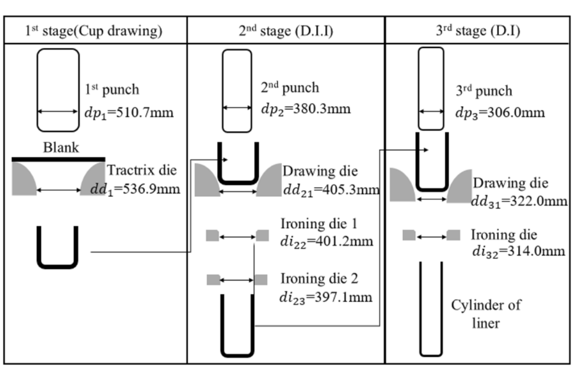

Figure 5 Dimensions of punches and dies calculated from the theoretical design rules of the D.D.I. process

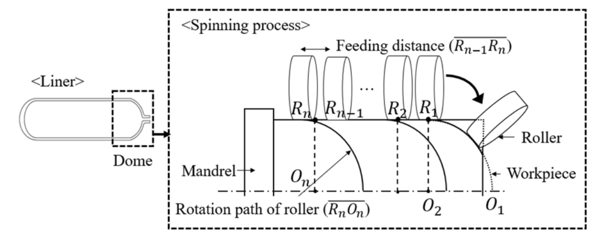

Figure 6 Spinning process to manufacture the dome part of liner

$$b_1 = \frac{D_0}{dm_1}, \tag{3}$$

$$dp_2 = dm_{21} - (1 + C_2) \times t_0, \tag{4}$$

$$dd_{21} = dm_{21} + (1 + C_2) \times t_0, \tag{5}$$

$$b_2 = \frac{dm_1}{dm_{2,1}}, \tag{6}$$

$$di_{23} = \sqrt{\frac{4A_{23}}{\pi} + dp_2^2}, \quad 0.5A_1 = A_{23}, \tag{7}$$

$$dp_3 = dm_{31} - (1 + C_3) \times t_{2,3}, \tag{8}$$

$$dd_3 = dm_{31} + (1 + C_3) \times t_{2,3}, \tag{9}$$

$$b_3 = \frac{dm_{23}}{dm_{31}} dm_{23} = \frac{dp_2 + di_{23}}{2}, \tag{10}$$

$$t_{23} = \frac{di_{23} - dp_2}{2} di_{32} = dp_3 + 2t_{32}. \tag{11}$$

A forming load (F) is computed by using effective stain ($\bar{\varepsilon}$), cross sectional area (A) and strain-flow stress equation of 34CrMo4 ($\bar{\sigma}$), shown in Eq. (12). Where the plastic modulus (K) is 90.42, and work hardening exponent (n) is 0.213. After finishing the D.D.I. process, dome part of the liner is formed through the hot spinning process. A cylinder of metal is rotated at high speed (1000 r/min), and a roller moves along the rotation path ($\overline{R_nO_n}$) and then back by feeding distance ($\overline{R_{n-1}R_n}$) as shown in Figure 6, finally, workpiece is formed into an axially symmetric dome part.

$$F = \bar{\sigma}A = K\overline{\varepsilon^n}A = KA \int \sqrt{2}/3\left\{(\mathrm{d}\varepsilon_r - \mathrm{d}\varepsilon_\theta)^2 + (\mathrm{d}\varepsilon_\theta - \mathrm{d}\varepsilon_z)^2 + (\mathrm{d}\varepsilon_z - \mathrm{d}\varepsilon_r)^2\right\}. \tag{12}$$

2.2 Filament Winding Process

Filament winding of the composite material, which involves winding filaments under tension over a rotating

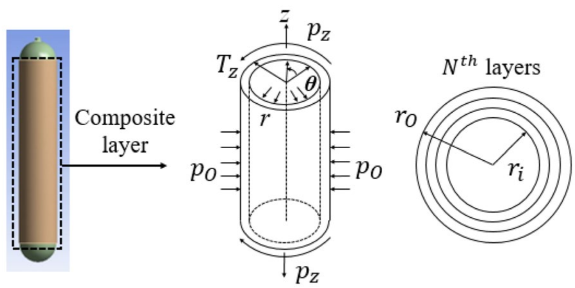

Figure 7 Mathematical model of multi-layered filament wound composite pressure vessel

mandrel, is a fabrication technique mainly used for manufacturing pressure vessels [12]. The liner is wound by E-glass with winding angle of 90°. The laminated composite pressure vessel is expressed in cylindrical coordinates with r (radial coordinate), θ (hoop coordinate) and z (axial coordinate) as illustrated in Figure 7. The differential equations relating to displacements (u) and stiffness constants ($\overline{C}$) are determined by Eqs. (13) and (14). $\tau_{\theta r}$ and τ_{zr} are obtained from Eq. (15). Where γ_0 has physical interpretation which is twist of vessel per unit length. The axial strain of all layers are equal to a constant ε_0, and $A(k)$ and $B(k)$ are unknown integration constants.

$$\frac{\mathrm{d}^2u_r^{(k)}}{\mathrm{d}r^2}+\frac{1}{r}\frac{\mathrm{d}u_r^{(k)}}{\mathrm{d}r}-\frac{\overline{C}_{22}^{(k)}/\overline{C}_{33}^{(k)}}{r^2}u_r^{(k)} =\frac{\overline{C}_{12}^{(k)}-\overline{C}_{13}^{(k)}}{\overline{C}_{33}^{(k)}}\frac{\varepsilon_0}{r}+\frac{\overline{C}_{26}^{(k)}-2\overline{C}_{36}^{(k)}}{\overline{C}_{33}^{(k)}}\gamma_0, \tag{13}$$

$$\frac{\mathrm{d}u_\theta^{(k)}}{\mathrm{d}r}-\frac{u_\theta^{(k)}}{r} =\frac{-\overline{C}_{55}^{(k)}}{\left(\overline{C}_{33}^{(k)}\right)^2-\overline{C}_{44}^{(k)}\overline{C}_{55}^{(k)}}\frac{A^{(k)}}{r^2}+\frac{\overline{C}_{45}^{(k)}}{\left(\overline{C}_{45}^{(k)}\right)^2-\overline{C}_{44}^{(k)}\overline{C}_{55}^{(k)}}\frac{B^{(k)}}{r}, \tag{14}$$

$$\tau_{\theta r}^{(k)}=A^{(k)}/r^2,\quad \tau_{zr}^{(k)}=B^{(k)}/r. \tag{15}$$

For the anisotropic materials, there exist $\overline{C_{22}}^{(k)}/\overline{C_{33}}^{(k)}>0$ and $\overline{C_{22}}^{(k)}/\overline{C_{33}}^{(k)}\neq 1$. If $\beta^{(k)}=\sqrt{\overline{C_{22}}^{(k)}/\overline{C_{33}}^{(k)}}$, the solution for Eqs. (13) and (14) is given by Eqs. (16), (17), where $D^{(k)}$ and $E^{(k)}$ are integration constants [13]:

$$u_r^{(k)}=D^{(k)}r^{\beta(k)}+E^{(k)}r^{-\beta(k)}+\alpha_1^{(k)}\varepsilon_0 r+\alpha_2^{(k)}\gamma_0 r^2, \tag{16}$$

$$\begin{aligned}\alpha_1^{(k)}&=\overline{C}_{12}^{(k)}-\overline{C}_{13}^{(k)}/\overline{C}_{33}^{(k)}-\overline{C}_{22}^{(k)},\\ \alpha_2^{(k)}&=\overline{C}_{26}^{(k)}-2\overline{C}_{36}^{(k)}/4\overline{C}_{33}^{(k)}-\overline{C}_{22}^{(k)}.\end{aligned} \tag{17}$$

The on-axis stiffness constants, $\left\{C_{ij}^{(k)}\right\}$, can be calculated using Eq. (18):

$$\left\{C_{ij}^{(k)}\right\}=\left\{C_{xx}^{(k)},C_{yy}^{(k)},C_{zz}^{(k)},C_{xy}^{(k)},C_{xz}^{(k)},C_{yz}^{(k)},C_{xx}^{(k)},C_{yy}^{(k)},C_{zz}^{(k)}\right\}^{\mathrm{T}}. \tag{18}$$

All the unknown integration constants in Eqs. (13) and (14) are determined by substituting these equations into boundary conditions. The traction pressure (p_0) at the inner surface and the traction-free condition at the outer surface are written as Eqs. (19) and (20). Where r_0 and r_a are the inner and outer radii, respectively.

$$\sigma_r^{(1)}(r_0)=-p_0,\quad \sigma_r^{(n)}(r_a)=0, \tag{19}$$

$$\begin{aligned}&\tau_{\theta r}^{(1)}(r_0)=\tau_{zr}^{(1)}(r_0)=0,\\ &\tau_{\theta r}^{(n)}(r_a)=\tau_{zr}^{(n)}(r_a)=0.\end{aligned} \tag{20}$$

Assuming that the interfaces between the core and skin layers are perfectly bonded, the continuity conditions for the displacement and stresses in the interfaces lead to Eqs. (21) and (22):

$$u_r^{(k)}(r_k)=u_r^{(k+1)}(r_k),\quad u_\theta^{(k)}(r_k)=u_\theta^{(k+1)}(r_k), \tag{21}$$

$$\begin{aligned}&\sigma_r^{(k)}(r_k)=\sigma_r^{(k+1)}(r_k),\\ &\tau_{zr}^{(k)}(r_k)=\tau_{zr}^{(k+1)}(r_k),\\ &\tau_{\theta r}^{(k)}(r_k)=\tau_{\theta r}^{(k+1)}(r_k).\end{aligned} \tag{22}$$

In addition, the axial equilibrium and the zero torsion condition for a cylinder with closed ends are expressed as Eq. (23):

$$2\pi\sum_{k=1}^{n}\int_{r_{k-1}}^{r_k}\sigma_z^{(k)}(r)r\mathrm{d}r=\pi r_0^2p_0,\quad 2\pi\sum_{k=1}^{n}\int_{r_{k-1}}^{r_k}\tau_{z\theta}^{(k)}(r)r^2\mathrm{d}r=0. \tag{23}$$

Substituting Eqs. (19) and (20) into Eqs. (13) and (14), the integration constants, $A^{(k)}=B^{(k)}=0$. Therefore, the solution for the hoop displacement (u_θ) is obtained from Eq. (24):

$$u_\theta^{(k)}=\gamma_0 rz. \tag{24}$$

Eqs. (19)–(23) give a set of equations to determine $2N+2$ unknown constants ($D^{(k)},E^{(k)}(k=1,2,\ldots,N)$, and ε_0,γ_0) for N-layered composite tube.

Tsai-Hill criterion shown in Eq. (25) is employed to characterize the failure of the composite materials (E-glass/epoxy) due to multiaxial loading conditions. Where X, Y, and Z are the yield strength in each direction, and Q, R and S are the shear strength in each direction.

$$\frac{\sigma_1^2}{X^2}+\frac{\sigma_2^2}{Y^2}+\frac{\sigma_3^2}{Z^2}-\sigma_1\sigma_2\left(\frac{1}{X^2}+\frac{1}{Y^2}-\frac{1}{Z^2}\right)-\sigma_1\sigma_3\left(\frac{1}{X^2}-\frac{1}{Y^2}+\frac{1}{Z^2}\right)$$
$$-\sigma_2\sigma_3\left(-\frac{1}{X^2}+\frac{1}{Y^2}+\frac{1}{Z^2}\right)+\frac{\sigma_4^2}{Q^2}+\frac{\sigma_5^2}{R^2}+\frac{\sigma_6^2}{S^2}=1. \tag{25}$$

2.3 Curing Process

After the filament winding process, curing process is performed to reinforce adhesive strength between composite layers to keep working pressure and structural safety of pressure vessel. The composite is cured in an IR oven to infuse liquid resin [14].

Temperature change of the vessel including thermal transmission and resin exothermic reaction, is a transient process. The thermal conductivity model is expressed as Eq. (26). Where ρ_r, v_r and $\dot{Q}_r$ are density, volume fraction and heat release rate of the resin, respectively [15].

$$\rho\dot{Q}=\rho_r v_r\dot{Q}_r. \tag{26}$$

Released heat quality of the resin is solved by the kinetics model of curing rate of the epoxy resin shown in Eqs. (27)–(29). H_r is the total heat of the reaction per unit mass released by curing process. $\mathrm{d}\alpha/\mathrm{d}t$ and α are curing rate and curing degree of resin, respectively. m and n are exponents, and k_1 and k_2 are defined by the Arrhenius rate expressions. A_1 and A_2 are pre-exponential coefficients, and ΔE_1 and ΔE_2 are activation energies. R is universal gas constant.

$$\dot{Q}_r=\frac{\mathrm{d}\alpha}{\mathrm{d}t}H_r, \tag{27}$$

$$\frac{\mathrm{d}\alpha}{\mathrm{d}t}=\left(k_1+k_2\alpha^m\right)(1-\alpha)^n, \tag{28}$$

$$k_1=A_1\exp\left(-\frac{\Delta E_1}{RT}\right),\quad k_2=A_2\exp\left(-\frac{\Delta E_2}{RT}\right). \tag{29}$$

The curing kinetics model is solved by finite difference method as shown in Eq. (30). It has been assumed that temperature in a period of time Δt is a constant so that the time integral method can be used to calculate a curing degree. αt is the known value of curing degree at the previous calculation [16, 17].

$$\alpha^{t+\Delta t}=\alpha^t+\left(\frac{\mathrm{d}\alpha}{\mathrm{d}t}\right)^{t+\Delta t}\Delta t. \tag{30}$$

The total residual strain ($\Delta\varepsilon$), considering the thermal residual strain of composite ($\Delta\varepsilon^{th}$) and the curing shrinkage residual strain ($\Delta\varepsilon^{ch}$) of the composite material, is computed by Eq. (31). Where γ (0.11) is the coefficient of composite thermal expansion and β (0.05) is the volume shrinkage ratio [18, 19].

$$\Delta\varepsilon=\Delta\varepsilon^{th}+\Delta\varepsilon^{ch}=\gamma\Delta T+\sqrt[3]{1+\beta\Delta\alpha}-1. \tag{31}$$

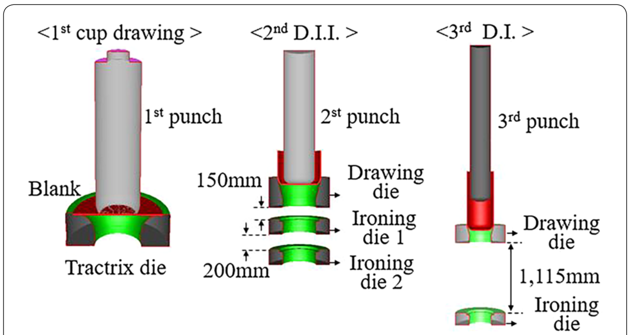

Figure 8 Analysis models in the D.D.I. process

3 Finite Element Analysis for Manufacturing Processes of the Composite Pressure Vessel-Type II

3.1 Finite Element Analysis of D.D.I. Process

To minimize forming load in the 1st deep drawing, design of tractrix die was conducted through FE analysis according to heights of the die. Forming analyses in the 2nd (D.I.I.) and the 3rd (D.I.) stages were performed with the results shown in Table 2, and the final liner shape (t_f=4 mm, D_{in}=306 mm) was obtained.

3.1.1 Modeling and Boundary Conditions

The D.D.I. process was simulated using commercial software, Forge NxT 2.0, and 3D modeling of an analysis model in each forming stage, which consists of a workpiece, a die and a punch, was conducted based on Tables 1 and 2 as shown in Figure 8. Distances between the dies were suggested in the actual filed, and tetrahedron meshes of the workpiece are generated. The workpieces are set to deformable domain, and the dies and punches rigid bodies. Strain-flow stress of 34CrMo4 according to the temperatures offered by Forge NxT 2.0 was adopted as shown in Figure 9. Friction coefficient (μ) and friction constant (m) are defined as 0.056 and 0.11, respectively [20]. Velocity of the punch is 50 mm/s, which is used in the actual field [21, 22].

Equation of tractrix curve, applied to the 1st deep drawing die, is shown in Eq. (32), where B is distance between asymptote and y-axis and a is shape factor. The height (h) of the tractrix die and inflow angle (θ) of

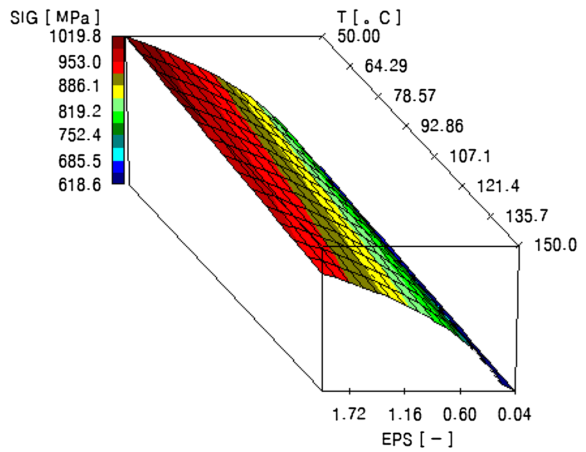

Figure 9 Strain-flow stress curve of 34CrMo4 according to the temperatures

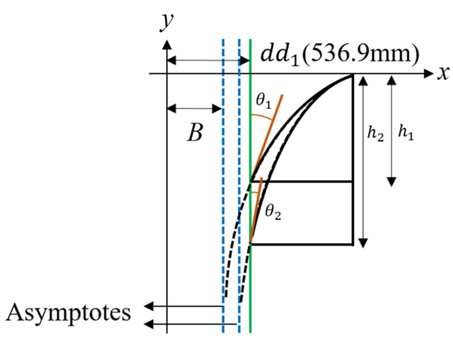

Figure 10 Shapes of tractrix die according to the heights

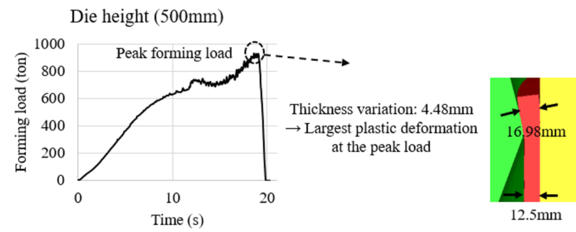

Figure 11 Forming loads according to the times (die height: 500mm)

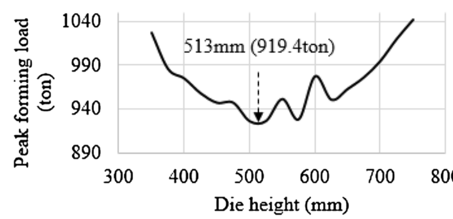

Figure 12 Peak forming load according to the die heights

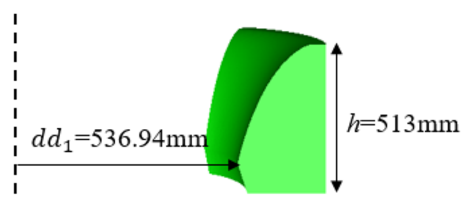

Figure 13 Suggested shape of the tractrix die with height of 513 mm

Table 3 Die height and inflow angle of material

Die height (mm)	Inflow angle (°)	Die height (mm)	Inflow angle (°)
375	18.1	575	7.8
400	15.2	600	7.1
425	13.6	625	6.4
450	12.2	650	5.7
500	10.9	700	5.2
525	9.8	725	4.8
550	8.8	750	4.5

blank change according to shape factor (a) as shown in Figure 10. To minimize forming load, design of the shape of tractrix die was implemented by varying die heights (375–750 mm) at the interval of asymptote (25 mm). Inflow angles of material according to die height are listed in Table 3, and dd_1 (536.94 mm) is fixed value in the basis of Table 2 [23–25].

$$x = B + \operatorname{sech}(t), \quad y = -a(t - \tanh(t)). \tag{32}$$

3.1.2 Result and Discussion

As the punch stroke proceeded, thicker sheet due to the amount of inflowing into the die causes the forming load to increase, and the peak load has the largest thickness variation during the drawing process as shown in Figure 11. Trend line of the peak forming load obtained by varying the die heights plotted in Figure 12 indicated that the load changes according to inflow angle of material and die height, and the minimum value, 919.4 t, was obtained at the height of 513 mm as shown in Figure 13.

In case of the die heights (375 mm to 513 mm), the forming load was decreased due to reduction of the maximum equivalent strain (375 mm: 2.04, 513 mm: 1.22) as shown in Figure 14. As the reduction of stain has a greater influence on forming load than the increase of the contact area, the forming load was decreased in the rages (550–575 mm and 600–625 mm), otherwise, the forming load was increased in the rages (513–550 mm and

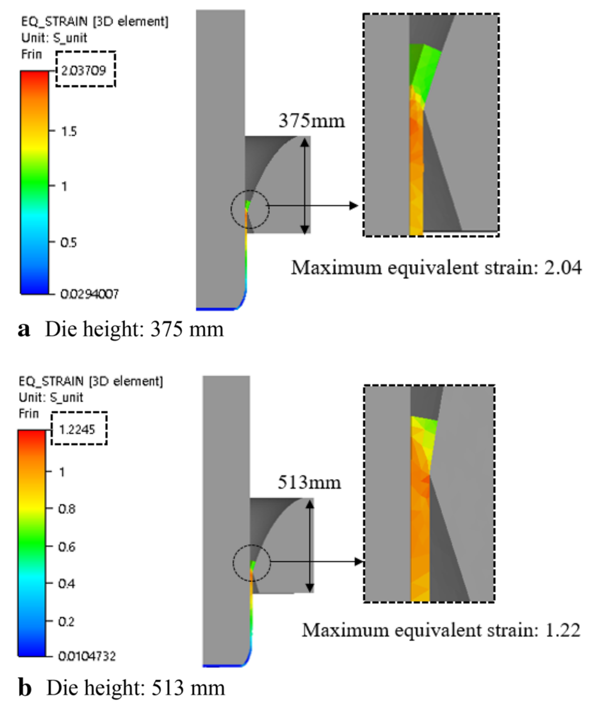

Figure 14 Equivalent strain distributions when the die heights are 375 mm and 513 mm

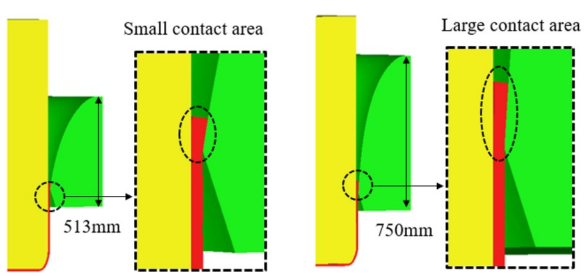

Figure 15 Contact areas when the die heights are 513mm and 750mm

575–600 mm), and fluctuations of the forming load were observed in the transition range (500–650 mm). After then (650–750 mm), the larger contact area allowed to increase the forming load as shown in Figure 15.

The workpiece shape obtained from the 1st deep drawing using the suggested tractrix die was imported to the initial billet of the 2nd stage with which forming analyses in the 2nd (D.I.I.) and the 3rd (D.I.) stages were performed based on the theoretical calculation results shown in Table 2. When the adjacent nodes overlap because of folding phenomenon, "Fold value" calculated form Forge NxT-Post processor is 1, otherwise, "Fold value" is 0. "Fold value" of the final workpiece shape in each stage is 0 as shown in Table 4, so that forming defects such as wrinkling and folding did not occur. The maximum forming loads of each stage were 919.4 t, 1030.5 t and 753.7 t, respectively, and the above values are below the press capacity (1500 t) used in the actual field, so feasibility of the D.D.I. process was confirmed.

Dimensions of the final liner shape obtained from after the 3rd stage process were compared with those of the desired product (t_f=4 mm, D_{in}=306 mm) shown in Table 1: Inner diameter (305.9 mm) measured from the *y*-coordinate of a node at inside surface of the cylinder part, the thickness (3.99 mm) as shown in Figure 16. The D.D.I. process design and FEA technique were verified through the above minor errors, 0.03% and 0.25% respectively.

3.2 Finite Element Analysis of Composite Layer

Thickness of the composite layer of the pressure vessel (Type II) was decided based on the results of static structural analyses using ACP (ANSYS Composite PrepPost).

3.2.1 Modeling and Boundary Conditions

3D model of the liner (t_f=4 mm, D_{in}=306 mm) and mechanical properties of 34CrMo4 were inputted in the Mechanical Model module as shown in Figure 17(a). In the ACP Pre module, anisotropic material properties, thickness and laminated angle (90°) of the E-glass fiber were set in the 3D modeling of the composite layer generated, as shown in Figure 17(b). Two models generated through above procedures were imported to the Static Structural module, and then pressure vessel (Type II) with liner and composite layer was created as shown in Figure 17(c). Equivalent stresses of the liner and the composite layer are obtained in the Static Structural module, and Tsai-Hill value to check failure of the composite layer are checked in ACP-Post module.

The internal pressure of 30.75 MPa, which is 1.5 times the working pressure (20.5 MPa), based on the Korea gas safety C016-2000 safety regulations, was imposed on the inner surface of the liner. When the CNG vessel is installed in the bus, inlet part is bolted to the valve, which does not allow to move all rotational and translational directions, including circumferential and axial directions. So the fully fixed support condition was applied to the upper surface of the inlet as shown in Figure 18.

3.2.2 Result and Discussion

Based on the international regulation, following requirements have to be taken into account to prevent fracture of composite pressure vessel, when being subjected to the internal pressure (30.75 MPa): Maximum equivalent stress of the liner < the yield strength of the liner (840.0

Table 4 Results of each forming stage

	Fold check of the final workpiece	Forming load according to time
1st stage (deep drawing)	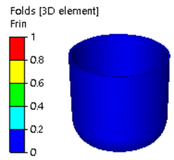	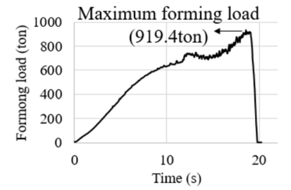
2nd stage (D.I.I.)	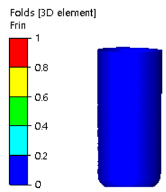	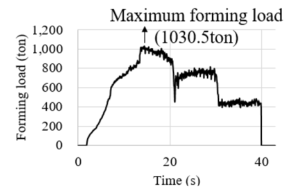
3rd stage (D.I.)	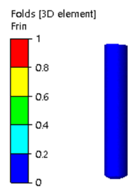	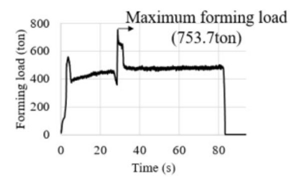

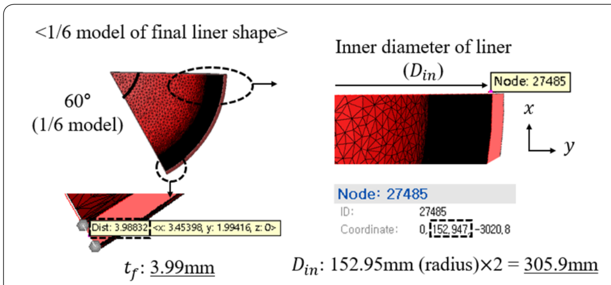

Figure 16 Dimensions of the final liner shape after 3rd stage

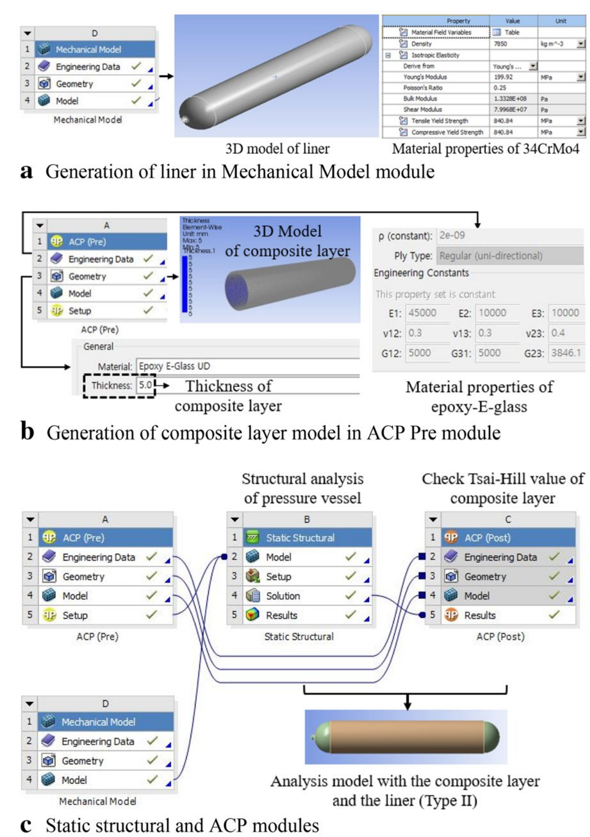

Figure 17 Static structural analysis of the pressure vessel (Type II) in the each module

MPa), maximum Tsai-Hill value of composite (Eq. (5)) < the critical value (1). The thinner composite layer is required to achieve weight lightening and cost reduction, and thickness (5–7 mm) of the composite layers for the Type II vessel is used in the actual field. So case study with different thicknesses (5 mm, 6 mm, 6.3 mm, 6.6 mm and 7 mm) was conducted to obtain better condition for structural safety and weight lightening as shown in Table 5.

The thickness of 6.3 mm, in which the maximum equivalent stress (834.2 MPa) is less than the yield strength (840.0 MPa)), and in which the maximum Tsai-Hill value (0.96) is less than the critical value (1), was chosen as shown in Figure 19.

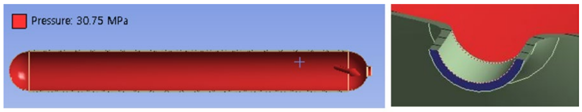

Figure 18 Load and boundary conditions of static structural analysis

Table 5 Results of structural analysis of liner and composite layer according to the thicknesses of composite layer

Thickness of composite layer (mm)	Maximum equivalent stress of liner (MPa)	Maximum Tsai-Hill value of composite layer
5	871.92	1.11
6	842.48	1.00
6.3	834.18	0.96
6.6	826.08	0.92
7	815.91	0.87

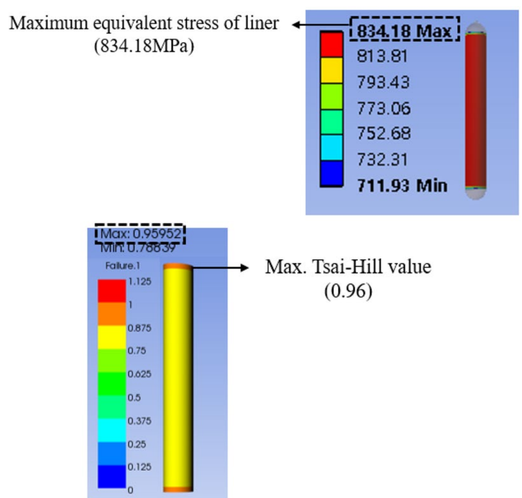

a Maximum equivalent stress of the liner and Tsai-Hill value of composite layer

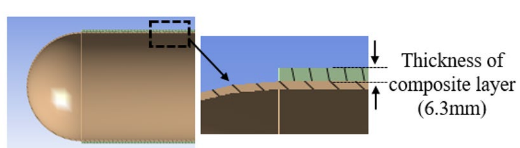

b Thickness of composite layer suggested

Figure 19 Results of static structural analysis in case of the thickness of composite layer (6.3 mm)

3.3 Finite Element Analysis of Curing Process

3.3.1 Modeling and Boundary Conditions

In order to compregnate the E-glass fibers on the liner, the epoxy resin and the fiber are laminated alternately as shown in Figure 20. The higher volume fraction of the fiber increases the longitudinal and the transverse Young's moduli (E_1 and E_2) and decreases the major Poisson's ratio (ν_{12}), which alleviates strain occurred due to the internal pressure. The high elasticity of the composite, which leads to larger compressive residual stress of the liner in the autofrettage process, reinforces strength and fatigue life of the high pressure vessel subjected to the working pressure (20.5 MPa) [26]. Also, the thermoplastic property of the composite improves as the volume fraction increases, this enhances resistance for deformation occurred due to the curing temperature.

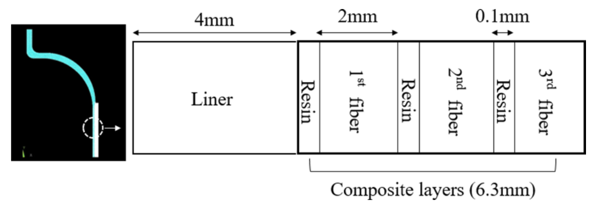

Figure 20 Analysis model of the curing process

Table 6 Material properties of E-glass fiber and resin

Property	E-glass fiber	Epoxy resin
Density (kg/m^3)	2540	1225
Specific heat (J/(kg·°C))	712	967
Thermal conductivity (W/(m·°C)	8.67	0.14
Elasticity modulus (Pa)	3.05×10^{11}	1×10^{9}
Poisson's ratio	0.2	0.3
Thermal expansivity (1/°C)	1.5×10^{-6}	2.5×10^{-6}

In the thermal analysis, the convection coefficient of 5 W/(m^2·°C) was adopted to the inner surfaces of the liner, and the curing temperature was applied to the outside surfaces of the liner and the composites, which were subjected to the external heat resource generated from the oven. In the stress & strain analysis, the fully fixed support condition was adopted to the upper surface of the inlet. The material properties of the E-glass fiber and epoxy resin are listed in Table 6.

Curing kinetics model offers the internal heat resource to the thermal conductivity model, and the temperature field of the composite is calculated by the thermal conductivity model, which influences on the curing rate of the resin, so both kinetics and thermal conductivity models were calculated at the same time, by using Eqs. (26)–(30) [14, 15]. The APDL code for iterative calculation of kinetic-thermal conductivity analysis is shown in Figure 21(a).

```
<Calculate curing degree and curing rate>
 *DO,ii,1,20,1
 DETLA1(ii)=A1*2.718**(-E1/(R*((nodetemp((ii)*50,1))+273)))
 DETLA2(ii)=A2*2.718**(-E2/(R*((nodetemp((ii)*50,1))+273)))
 da(ii)=DETLA1(ii)+A2*2.718**(-E2/(R*((nodetemp((ii)*50,1))+273)))
        *DEGREE**m)*(1-DEGREE)**n
 DEGREE=DEGREE+(da(ii))*50
 *ENDDO

<Calculate internal heat resource released by resin >
 qheat(iii,1)=Hr*da(ii)

 *ENDDO

<Judge curing degree is 1 or not>
 *if,DEGREE,GE,1,THEN
 DEGREE=1
 *ELSE
 *ENDIF
```

a Kinetic-thermal conductivity analysis

```
<Calculate total residual strain >

 NODEDGSTRAIN(iii,1)=(1+C*DEGREE)**(1/3)-1

 NODECMSTRAIN(iii,1)=B*nodetemp(ii*50)-(1+C*DEGREE)**(1/3)-1
 strainatnode(1,1)=B*nodetemp(ii*50)-(1+C*DEGREE)**(1/3)-1
```

b Thermal-structural coupled analysis

Figure 21 APDL code to simulate curing analysis

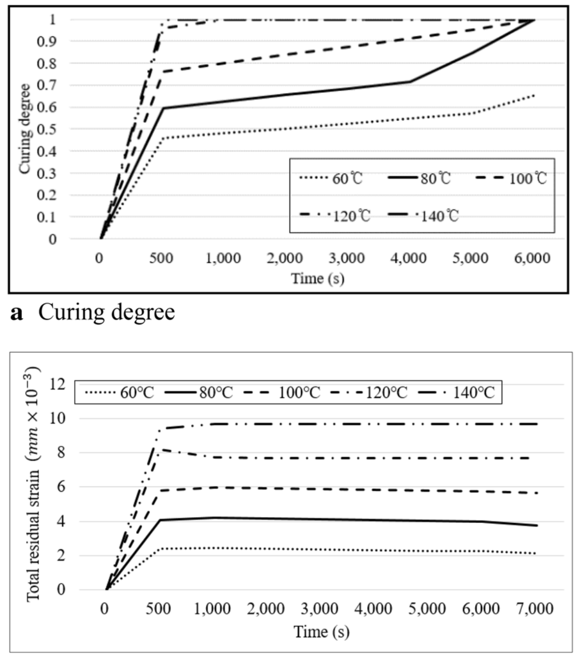

a Curing degree

b Total residual strain

Figure 22 Results of curing analyses according to the temperatures of external heat resource

In the first calculation, the initial temperature (30 °C), the initial curing degree ($\alpha = 0$), the curing kinetic parameters of epoxy resin and external heat resource were inputted. Curing degree (α_1) was computed by using kinetics model, and then internal heat resource released by the resin ($Q_{r,1}$) and the temperature field (T_1) by the external heat were calculated by using thermal conductivity model. The outputs of 1st calculation (α_1, $Q_{r,1}$ and T_1) are to be input parameters of 2nd calculation, and the above mentioned calculation processes were repeated. When the value of curing degree is less than 1, the program continually calculates curing degree and released heat, which are defined as the initial value for next calculation. In order to calculate total residual strain of the composite layer, thermal-structural coupled field analysis is conducted by transference of temperature field and curing degree. Based on APDL code illustrated in Figure 21(b), total residual strain considering thermal and curing shrinkage phenomenon was computed by using Eq. (31) [27, 28].

3.3.2 Result and Discussion

Curing analyses were implemented according to the three design parameters; temperatures of external heat resource (60 °C, 80 °C, 100 °C, 120 °C and 140 °C) [29], the number of heating stages (two stages, three stages, four stages and five stages) [30] and heating rates at the second stage (0.0075 °C/s, 0.015 °C/s, 0.02 °C/s, 0.03 °C/s and 0.04 °C/s) [31]. The external starting temperature of first step is fixed to 80 °C. The analysis results according the temperature of the external heat resource indicated that the high constant temperature enables the curing process to be completed more quickly, and even if the external temperature is low, the curing degree reaches 1 when the heating time is long enough as shown in Figure 22. Based on the analysis results according to the number of heating stage, the curing processes with 4 and 5 heating stages have not been reached to 1, and this means they have not been completed within the inputted curing time. But, the higher the number of heating stage is, the lower maximum strain is as shown in Figure 23. Higher heating rate accelerated the curing process, and the differences between the maximum total residual strains were small as shown in Figure 24. Considering the results of curing analyses, the best curing conditions to reduce the maximum residual strain and to reach the curing degree ($\alpha = 1$) in a short time were suggested in Table 7.

4 Conclusions

In this study, an integrated design method (D.D.I., spinning, filament winding and curing processes) to manufacture the CNG composite pressure vessel (Type II) ($t_f = 4$ mm, $D_{in} = 306$ mm, $D_{out} = 314$ mm and $L = 1830$ mm) was presented to ensure structural safety and to reduce production costs. The summaries are as follows.

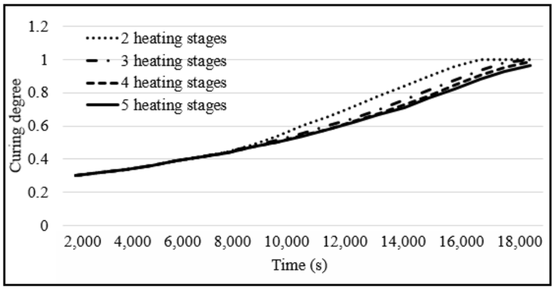

a Curing degree

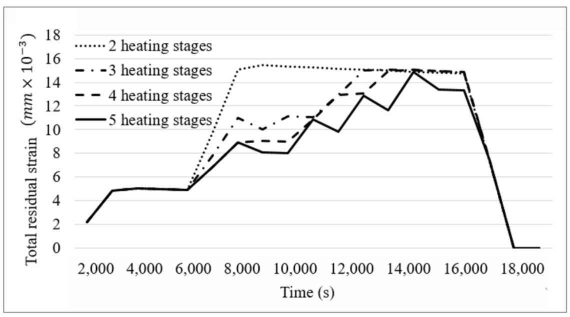

b Total residual strain

Figure 23 Results of curing analyses according to the number of heating stages

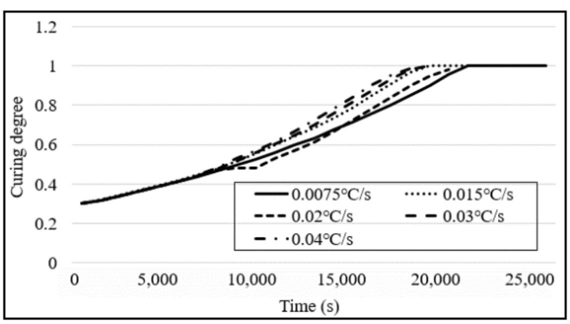

a Curing degree

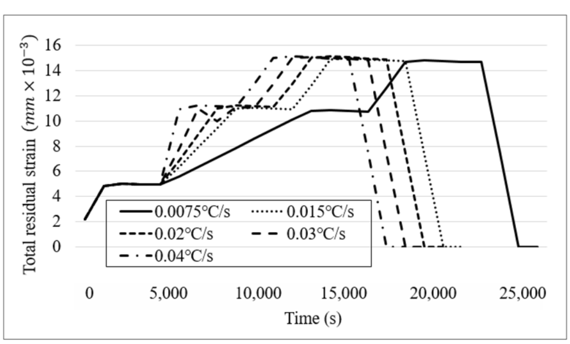

b Total residual strain

Figure 24 Results of curing analyses according to the heating rates

Table 7 Best curing conditions of the pressure vessel

	1st heating stage	2nd heating stage	3rd heating stage
Temperature (°C)	80	140	180
Heating rate (°C/s)	0.04	0.03	0.02
Heating time (s)	0–2000	5000–7000	10000–12000

1) Dimensions of the dies and the punches are theoretically calculated by applying the design rules of the D.D.I. process. ($dp_1 = 510.69$ mm, $dd_1 = 536.94$ mm, $dp_2 = 380.25$ mm, $dd_{21} = 405.25$ mm, $di_{22} = 401.19$ mm, $di_{23} = 397.10$ mm, $dp_3 = 306.00$ mm, $dd_{31} = 322.00$ mm, $di_{32} = 314.00$ mm). Design of the tractrix die was conducted to improve die life and reduce manufacturing costs (height = 513 mm).
2) The thickness of the composite layer to ensure structural safety and minimum use of material was chosen as 6.3 mm to have the maximum equivalent stress of the liner (834.18 MPa), which do not exceed the yield strength (840 MPa), and the maximum value of Tsai-Hill is 0.96, which is below critical value of 1.
3) The curing conditions (1st stage: 80 °C, 0.04 °C/s, 0–2000 s, 2nd stage: 140 °C, 0.03 °C/s, 5000–7000 s, 3rd stage: 180 °C, 0.02 °C/s, 10000–19000s) to complete curing process in a short time with low residual strain were suggested.

Authors' Contributions

HK designed and debugged the analyses and wrote the manuscript; GP and HS assisted with FEA analyses; CK was in charge of the whole trial. All authors read and approved the final manuscript.

Authors' Information

Hyoseo Kwak received her B.S. and M.S. degrees from School of Creative Engineering and a Ph.D. degree in Mechanical Convergence Technology from Pusan National University, Korea, in 2012, 2014, and 2017, respectively. She is currently a Research at the Research Institute of Mechanical Technology, Pusan National University, Korea. Her research interests include machine design and FEM simulation (forming, structures, dynamics, and fluid analyses).

Gunyoung Park received his B.S. degree from School of Mechanical Engineering, Pusan National University, Korea. Now he is studying for the master course in Mechanical Convergence Technology at Pusan National University, Korea. His research interests include machine design and FEM simulation (forming, structure analyses).

Hansaem Seong received B.S. degree from School of Mechanical Engineering and M.S. degree from Mechanical Convergence Technology. Now he is studying for the doctorate in Mechanical Convergence Technology at Pusan National University, Korea. His research interests include machine design and FEM simulation (forming, structures, and thermal analyses).

Chul Kim received his M.S. and Ph.D. degrees in 1987 and 1997. Professor Kim is currently a Professor at the Research Institute of Mechanical Technology of Pusan National University, Korea. His research fields include FEM simulation (structures, dynamics, and fluid analysis), optimal structural design, and CAD/CAM.

Acknowledgements
The authors would like to express gratitude to National Research Foundation of Korea (NRF) for funding and NK Co., Ltd. for critical discussion and technical assistance.

Competing Interests
The authors declare that they have no competing interests.

Funding
Supported by National Research Foundation of Korea (NRF) and Korea Government (MSIT) (Grant No. 2019R1F1A1058521).

Author Details
[1] Research Institute of Mechanical Technology, Pusan National University, Pusan 609-735, Korea. [2] Department of Mechanical Convergence Technology, Pusan National University, Pusan 609-735, Korea. [3] School of Mechanical Engineering, Pusan National University, Pusan 609-735, Korea.

Received: 16 January 2019 Revised: 6 July 2019 Accepted: 24 September 2019
Published online: 23 October 2019

References
[1] P Gąsior, M Malesa, J Kaleta, et al. Application of complementary optical methods for strain investigation in composite high pressure vessel. *Composite Structures*, 2018, 203(1): 718-724.
[2] I Karen, N Kaya, ÖZTÜRK, et al. Intelligent die design optimization using enhanced differential evolution and response surface methodology. *Journal of Intelligent Manufacturing*, 2015, 26(5): 1027-1038.
[3] R Narayanasamy, C Loganathan. Study on wrinkling limit of commercially pure aluminum sheet metals of different grades when drawn through conical and tractrix dies. *Materials Science and Engineering: A*, 2006, 419(1-2): 249-261.
[4] P Geng, J Z Xing, X X Chen. Winding angle optimization of filament-wound cylindrical vessel under internal pressure. *Archive of Applied Mechanics*, 2017, 87(3): 365-384.
[5] L Zu, H Xu, H Wang. Design and analysis of filament-wound composite pressure vessels based on non-geodesic winding. *Composite Structures*, 2019, 207(1): 41-52.
[6] S Minakuchi, S Niwa, K Takagaki, et al. Composite cure simulation scheme fully integrating internal strain measurement. *Composites Part A: Applied Science and Manufacturing*, 2016, 84: 53-63.
[7] N Li, Y Li, J Jelonnek, et al. A new process control method for microwave curing of carbon fibre reinforced composites in aerospace applications. *Composites Part B: Engineering*, 2017, 122: 61-70.
[8] J H Bae, H W Lee, C Kim. A study on integrated design for manufacturing processes of a compressed natural gas composite vessel. *International Journal of Precision Engineering and Manufacturing*, 2014, 15(7): 1311-1321.
[9] S T Atul, M L Babu. A review on effect of thinning, wrinkling and spring-back on deep drawing process. *Proceedings of the Institution of Mechanical Engineers, Part B: Journal of Engineering Manufacture*, 2019, 233(4): 1011-1036.
[10] J P G Magrinho, C M A, Silva, M B Silva, et al. Formability limits by wrinkling in sheet metal forming. *Proceedings of the Institution of Mechanical Engineers, Part L: Journal of Materials: Design and Applications*, 2018, 232(8): 681-692.
[11] J H Bae, H W Lee, M S Kim, et al. Optimal process planning of CNG pressure vessel by ensuring reliability and improving die life. *Transactions of the Korean Society of Mechanical Engineers A*, 2013, 37(7): 865-873.
[12] M Xia, H Takayanagi, K Kemmochi. Analysis of multi-layered filament-wound composite pipes under internal pressure. *Composite Structures*, 2001, 53(4): 483-491.
[13] T R Tauchert. Optimum design of a reinforced cylindrical pressure vessel. *Journal of Composite Materials*, 1981, 15(5): 390-402.
[14] S Nakouzi, F Berthet, Y Maoult, et al. Simulations of an infrared composite curing process. *Advanced Engineering Materials*, 2011, 13(7): 604-608.
[15] T A Bogetti, J W G Jr. Two-dimensional cure simulation of thick thermosetting composites. *Journal of Composite Materials*, 1991, 25(3): 239-273.
[16] R Hardis, J L Jessop, F E Peters, et al. Cure kinetics characterization and monitoring of an epoxy resin using DSC, Raman spectroscopy, and DEA. *Composites Part A: Applied Science and Manufacturing*, 2013, 49: 100-108.
[17] M Rudolph, C Naumann, M Stockmann. Degree of cure definition for an epoxy resin based on thermal diffusivity measurements. *Materials Today: Proceedings*, 2016, 3(4): 1144-1149.
[18] S Yi, H H Hilton, M F Ahmad. A finite element approach for cure simulation thermosetting matrix composite. *Computers and Structures*, 1997, 64(1-4): 383-388.
[19] R Hardis. *Cure kinetics characterization and monitoring of an epoxy resin for thick composite structures*. Iowa States: Iowa State University, 2012.
[20] K O Lee, H D Sim, H S Kwak, et al. Optimal design of the tractrix die used in the DDI process for manufacturing CG pressure vessels. *The Korean Society of Mechanical Engineers*, 2016, 40(10): 879-886.
[21] Angasu Gonfa, K Srinivasulu. Deep drawing process parameters: A review. *International Journal of Current Engineering and Technology*, 2016, 6(4): 1204-1215.
[22] A R Joshi, K D Kothari, L Jhala. Effects of different parameters on deep drawing process: Review. *International Journal of Engineering Research & Technology (IJERT)*, 2013, 2(3): 1-5.
[23] R K Kesharwani, S Basak, S K Panda, et al. Improvement in limiting drawing ratio of aluminum tailored friction stir welded blanks using modified conical tractrix die. *Journal of Manufacturing Processes*, 2017, 28(1): 137-155.
[24] R Pernis, I Barényi, J Kasala, et al. Evaluation of limiting drawing ratio (LDR) in deep drawing process. *Acta Metallurgica Slovaca*, 2015, 21(4): 258-268.
[25] M P Henriques, R J Alves de Sousa, R A F Valente. Numerical simulation of wrinkling deformation in sheet metal forming. *7th EUROMECH Solid Mechanics Conference*, Lisbon, Portugal, 2009: 7–11.
[26] Z H Hu, R G Wang, X D He, et al. Numerical simulation of residual strain/stress for composite laminate during overall curing process. *Journal of Aeronautical Material*, 2008, 2: 001.
[27] C Li, Liu, M H Liu, Z Y Liu, et al. DSC and curing kinetics of epoxy resin using cyclohexanediol diglycidyl ether as active diluents. *Journal of Thermal Analysis and Calorimetry*, 2014, 116(1): 411-416.
[28] R L Pagano, V M A Calado, F W Tavares, et al. Parameter estimation of kinetic cure using DSC non-isothermal data. *Journal of Thermal Analysis and Calorimetry*, 2011, 103(2): 495–499.
[29] M Sudheer, K R Pradyoth, S Somayaji. Analytical and Numerical validation of epoxy/glass structural composites for elastic models. *American Journal of Materials Science*, 2015, 5(3C): 162-168.
[30] M Hojjati, S V Hoa, Curing simulation of thick thermosetting composites. *Composites Manufacturing*, 1994, 5(3): 159-169.
[31] J Zhang, Y C Xu, P Huang. Effect of cure cycle on curing process and hardness for epoxy resin. *Express Polymer Letters*, 2009, 3(9): 534-541.